# Effects of heat treatment on the ballistic properties of AA6070 aluminium alloy

J. K. Holmen[a], J. Johnsen[a], S. Jupp[b], O.S. Hopperstad[a] and T. Børvik[a,c,*]

[a] *Structural Impact Laboratory (SIMLab), Centre for Research-based Innovation (CRI) and Department of Structural Engineering, Norwegian University of Science and Technology, NO-7491 Trondheim, Norway.*

[b] *Hydro Rolled Products GmbH, Research & Development, D-53117 Bonn, Germany*

[c] *Norwegian Defence Estates Agency, Research and Development Section, NO-0015 Oslo, Norway*

**Abstract**

The ballistic properties of the aluminium alloy AA6070 in different tempers are studied, using target plates of 20 mm thickness in tempers O (annealed), T4 (naturally aged), T6 (peak strength) and T7 (overaged). The stress-strain behaviour of the different tempers was characterised by quasi-static tension tests and was found to vary considerably with temper in regards to strength, strain hardening and ductility. Ballistic impact tests using 7.62 mm APM2 bullets were then carried out, and the ballistic limit velocities were obtained for all tempers. In the material tests it was shown that the O-temper was most ductile and almost no fragmentation took place during the ballistic impact tests. The T6-temper proved to be least ductile, and fragmentation was commonly seen. The experiments show that despite fragmentation, strength is a more important feature than ductility in ballistic impact for this alloy, at least for the given projectile and within the velocity range investigated. A thermoelastic-thermoviscoplastic constitutive relation and a ductile fracture criterion were determined for each temper, and finite element analyses were performed using the IMPETUS Afea Solver with fully integrated 3rd-order 64-node hexahedrons. The numerical simulations predicted the same variation in ballistic limit velocity with respect to temper condition as found in the experiments, but the results were consistently to the conservative side. In addition, analytical calculations using the cylindrical cavity expansion theory (CCET) were carried out. The ballistic limit velocities resulting from these calculations were found to be in good agreement with the experimental data.

*Keywords*: *Small-arms bullets; Aluminium armour; Ballistic impact tests; 3D numerical simulations; Cylindrical cavity expansion theory*

## 1. Introduction

Mobile protective structures are often made of thin plates of high-strength steel because of its excellent combination of strength, ductility, price and formability [1]. Aluminium alloys

* Corresponding author. Tel.: + 47-73-59-46-47; fax: + 47-73-59-47-01.

*E-mail address*: tore.borvik@ntnu.no (T. Børvik).

are also considered for armour applications owing to their high strength-to-density ratio (see e.g. [2]-[13]). Recent studies have indicated that high-strength aluminium alloys may have equally good or even better perforation resistance than steel when areal mass is taken into account [14][15], while other studies have suggested that the ballistic properties of plates are not only dependent on material strength but also on local ductility [16][17]. Since high-velocity perforation is an extremely localised process, the consequence is that structural materials with a balanced combination of strength and ductility may under certain conditions be superior energy absorbers for ballistic impact applications compared to special alloys having higher strength at the expense of ductility. Aluminium alloys can through alloying and heat treatments gain a number of useful properties with respect to perforation resistance [18], possibly making aluminium alloys an interesting alternative for protective structures.

In this study, the ballistic properties of the high-strength aluminium alloy AA6070 in different tempers have been investigated. Plates of 20 mm thickness were first produced by casting and hot-rolling at the Hydro Research Laboratory in Bonn, Germany, before they were heat treated to tempers O (annealed), T4 (naturally aged), T6 (peak strength) and T7 (overaged). This manipulation of the wrought alloy significantly changed the mechanical properties of the material, while retaining the grain structure. The stress-strain behaviour of the different tempers was characterised by conducting quasi-static tension tests at room temperature. The anisotropy in flow stress and fracture strain of the materials was obtained from tests in three different in-plane directions. Based on the material tests, a thermoelastic-thermoviscoplastic constitutive relation and a ductile fracture criterion were determined for each temper. Ballistic impact tests using 7.62 mm APM2 bullets were then carried out, and the ballistic limit velocities were obtained. In the material tests it was shown that the O-temper was the most ductile and almost no fragmentation took place in the ballistic tests. The T6-temper proved to be less ductile, and fragmentation during impact was commonly seen. It was found also for this alloy that strength is a more important feature than ductility in ballistic impact, at least within the limitations of this study. Finite element analyses were performed using the IMPETUS Afea Solver [19] with fully integrated 3$^{rd}$-order 64-node hexahedrons. Ballistic limit velocities were calculated on the basis of the numerical results and compared to the experimental values. The numerical simulations predicted the same variation in ballistic limit velocity with respect to temper condition as observed in the experiments, but the results were consistently to the conservative side. Finally, analytical calculations using the cylindrical cavity expansion theory (CCET) were performed. These results were found to be in good agreement with the experimental data.

## 2. Experimental study

### *2.1. Target and bullet materials*

Plates of the aluminium alloy AA6070 from Hydro are considered in this study. The chemical composition of the alloy can be found in Table 1. The melt was first DC-cast (direct chilled) to a thickness of 126 mm, then machined to 103 mm, homogenised at 550 °C for 4 hours before it was hot-rolled to a thickness of 20 mm. After production of the plates different heat treatments were applied to obtain tempers O (annealed), T4 (naturally aged), T6 (peak strength) and T7 (overaged), which gave a range of different strength and hardening properties to the alloy. The various steps in the heat treatment processes are described in Table 2. These heat treatments are not expected to change the grain structure of the material [18], as also confirmed by the tri-planar optical micrographs in Figure 1 showing the grain structure after heat treatments to temper O and T6.

Quasi-static tensile tests were carried out using smooth axisymmetric specimens with a gauge length of 40 mm and a cross-section diameter of 6 mm (Figure 2). The tensile axes of the specimens were oriented at 0°, 45° and 90° with respect to the rolling direction (RD) of the plate, and three repeat tests were carried out in each direction at room temperature (giving a total of 36 tests). The cross-head velocity of the test machine was 1.2 mm/min, corresponding to an average strain rate before necking of $5\times10^{-4}$ s$^{-1}$. The force and diameter at minimum cross-section of the specimen were continuously measured until fracture. The latter was made possible using a meter with two perpendicular lasers that accurately measured the specimen diameter. The lasers were installed on a mobile frame to ensure that the diameter during straining was always measured at minimum cross-section. The specimen diameter was measured in the thickness direction ($D_Z$) of the plate and in the transverse direction ($D_\perp$) of the specimen. The Cauchy (true) stress and the logarithmic (true) strain were calculated as

$$\sigma = \frac{F}{A}, \quad \varepsilon = \ln\frac{A_0}{A} \tag{1}$$

where $F$ is the force, $A_0 = \pi D_0^2/4$ is the initial cross-section area and $D_0$ is the initial diameter of the gauge section. The current area of the cross-section is given as

$$A = \frac{\pi}{4} D_Z D_\perp \tag{2}$$

The plastic strain is then obtained as $\varepsilon^p = \varepsilon - \sigma / E$, where $E$ is Young's modulus. Note that plastic incompressibility and negligible elastic strain have been assumed in Eq. (1). Since there might be variations in stress and strain over the cross-section, $\sigma$ and $\varepsilon$ should be considered as average values.

Typical true stress-strain curves to fracture are shown in Figure 3 (since the spread in experimental results between repeat tests was found to be negligible), while some material data are given in Table 3. Here $s_0$ is the 0.2% offset yield stress, $s_u$ is the ultimate tensile strength, $\sigma_{pt}$ is the true peak stress, $\varepsilon_f$ is the true failure strain and $W_c$ is the plastic work to failure given as the area under the true stress-strain curve (i.e. the Cockcroft-Latham parameter that will be further discussed in Section 3). The effects of the heat treatment are found to be significant, and considerable variation in yield stress, strain hardening and strain to failure with temper is observed. The general trends are that the anisotropy in flow stress of AA6070 is negligible, while the anisotropy in ductility is significant. The annealed O-temper is considerably more ductile than the other tempers. The fracture strain in the rolling direction is more than 3 times as high as for temper T6, while in the 90° direction it is more than 16 times as high. The opposite trends are seen for the strength. Temper T6 has a yield stress almost 8 times the O-temper. The yield stress is about 10% lower for temper T7, while temper T4 has only half the yield stress of temper T6. However, the strain hardening in temper T4 is much stronger than for the other tempers. Figure 3 and Table 3 further confirm that increased strength takes place at the expense of ductility. Temper T4 exhibits the highest $W_c$ value independent of specimen direction due to the balanced combination of strength and ductility.

The plates were impacted by APM2 bullets fired at various velocities. The 7.62 mm diameter, $10.5 \pm 0.25$ g mass, bullet consists of a brass jacket, a lead tip and a $5 \pm 0.25$ g, ogival-nose, hardened steel core with a calibre-radius-head of 3 and a Rockwell C hardness of 63. The purpose of the lead tip is to stabilize the bullet during flight and in the initial stage of penetration. Figure 4 shows the dimensions and the various parts that make up the APM2 bullet. More information regarding the bullet materials can be found in Børvik et al. [1].

### *2.2. Experimental set-up*

The ballistic impact tests were carried out in a compressed gas-gun facility described in detail by Børvik et al. [20][21]. A $7.62\times63$ mm specially designed smooth-bored Mauser rifle with a barrel length of about 1 m was in this study used to fire the APM2 bullets. The stock was removed and the rifle was mounted in a rigid rack inside the impact chamber of the gas-gun. This fixture guaranteed a well-defined impact point in all tests, and the rifle could be fired by a magnetic trigger from a safe distance. Square target plates of AA6070 with in-plane dimensions of 300 mm and thickness of 20 mm were firmly clamped to a rigid frame by two beams. This provided a fixed boundary for the horizontal sides of the targets, while the vertical sides remained free. The in-plane distance between each impact point and the target boundary was roughly 100 mm. Striking and residual velocities were measured with various laser optical devices that have been found to be accurate to within 1-2% [1]. In addition, the overall perforation process was photographed with a Photron FASTCAM SA1.1 high-speed video camera. To tune the impact velocity, the ammunition was adjusted so that the bullet impacted the target at velocities well above and just below the ballistic limit. Even though this was done with great care, some spread in initial impact velocity was found. Taking this uncertainty into account, six to nine tests had to be conducted for each temper to get an accurate prediction of the ballistic limit velocity.

### *2.3. Experimental results*

Based on a number of experimental tests, the ballistic limit curve and the ballistic limit velocity for each temper of the 20 mm thick AA6070 target plates have been determined. Measured initial ($v_i$) versus residual ($v_r$) velocities of the bullet from each experiment are plotted in Figure 5. The solid lines through the data points are fitted using a generalized version of the Recht-Ipson model [22] given as

$$v_r = a\left(v_i^p - v_{bl}^p\right)^{1/p} \tag{3}$$

where $a$ and $p$ may be taken as empirical constants, and $v_{bl}$ is the ballistic limit velocity. Since the bullets mainly pierced the plates by ductile hole growth, $a$ was chosen equal to unity (although some fragments were ejected from one or both surfaces of the target at the highest impact velocities), while $p$ and $v_{bl}$ were fitted to the test data using the method of

least squares. Obtained values of $a$, $p$ and $v_{bl}$ are given in Table 4. Even though some spread is seen (Figure 5), the agreement between the experimental data points and the Recht-Ipson model is good. The data further indicates a strong and rather linear increase in perforation resistance with target yield stress, and the results are in this sense in close agreement with similar data reported in [1] for steel plates. This confirms that the material strength is a more important feature than the measured strain to failure in the design of protective structures against small-arms bullets (as will be further discussed in Section 5).

Figure 6a) shows high-speed video images from the perforation process of a 20 mm thick plate in temper O at maximum impact velocity. Some fragmentation from the rear-side of the target plate is clearly seen. Note that the brass jacket enclosing the steel core of the bullet survived the test (see also Figure 15a)). Similar high-speed video images at medium impact velocity are given in Figure 6b). The impact velocity is considerably lower in this test, and no fragmentation of significance is seen during perforation. Inspection of the bullet holes after each test confirmed that no fragmentation took place in the O-temper at the lowest impact velocities, but small petals were formed on both sides of the cavity. This behaviour was as expected for a relatively ductile material as the annealed aluminium alloy. High-speed video images of the perforation process of a 20 mm thick plate in temper T6 at maximum and medium impact velocities are shown in Figure 7. The T6-temper exhibited the highest yield stress, but also the lowest fracture strain (see Figure 3), and this behaviour revealed itself in the ballistic tests through a higher degree of fragmentation during perforation. A similar behaviour was observed during impact of the high-strength aluminium alloy AA7075-T651 as described in [16][17]. It is also worth noting that as the impact velocity decreased, the front-side fragmentation increased and the rear-side fragmentation decreased (albeit some fragmentation on the rear side was still present). Only small pitch/yaw angles (below 1-2%) were registered in these tests (see e.g. the high-speed camera images in Figure 6 and Figure 7). Such small angles are assumed not to affect the ballistic limit of the target material. From the experimental results reported by Goldsmith [23], it appears that the penetration process is hardly affected by total yaw angles up to 3–5%. Larger yaw angles may, on the other hand, significantly reduce the penetration capacity of the projectile.

Cross-sections of sliced plates in temper O and T6 after impact are shown in Figure 8 and Figure 9, respectively. The transition from rear-side fragmentation to front-side fragmentation with a decrease in impact velocity is clearly illustrated in Figure 9. In the centre part of the plates, the cavities are mostly smooth and of circular shape, indicating penetration by ductile

hole growth. The more ductile failure mode of the O-temper can clearly be seen in Figure 8 when comparing it to the cross-sections of the T6-temper in Figure 9. Note that even though the impact in general was orthogonal (see e.g. Figure 6b)), a distinct obliquity developed during the perforation process (Figure 8b)) in some of the tests. Temper T4 and T7 have strength and hardening properties that lie between temper O and T6, and their behaviour during impact was a mixture of these two extremes. Temper T4 exhibited more petalling than the other tempers. Fragmentation was found to be important at the highest impact velocities for the least ductile tempers (T6 and T7), while ductile hole growth was dominating in the more ductile tempers (O and T4) and at the lowest impact velocities. Due to this, the fragmentation process is believed to have a relatively small effect on the ballistic limit velocity in this study. It should however be mentioned that for other impact conditions than those studied here (see e.g. [16]) the effect of target fragmentation may be essential.

## 3. Finite element simulations

### *3.1. Constitutive relation and fracture criterion*

A modified version of the Johnson-Cook (MJC) constitutive relation was used to model the target materials (see [1][24][25]). The constitutive behaviour is assumed to be isotropic and modelled with the von Mises yield criterion even though the materials exhibit some anisotropy (but mainly in the strain to failure, see Figure 3). The equivalent stress is then expressed as

$$\sigma_{eq} = \left( A + \sum_{i=1}^{2} Q_i \left( 1 - \exp\left( -C_i \varepsilon_{eq} \right) \right) \right) (1 + \dot{\varepsilon}_{eq}^{*})^{c} (1 - T^{*m}) \tag{4}$$

where $\varepsilon_{eq}$ is the equivalent plastic strain and $\left( A, Q_1, C_1, Q_2, C_2, c, m \right)$ are model parameters. Note that the usual power law strain hardening in Eq. (4) has been replaced by a two-term Voce strain hardening law (see e.g. [26]) for the target material in this study, since the latter generally gives a better fit of the stress-strain curve for aluminium alloys. The dimensionless plastic strain rate is given by $\dot{\varepsilon}_{eq}^{*} = \dot{\varepsilon}_{eq} / \dot{\varepsilon}_0$, where $\dot{\varepsilon}_0$ is a user-defined reference strain rate. The homologous temperature is defined as $T^{*} = \left( T - T_r \right) / \left( T_m - T_r \right)$, where $T$ is the absolute

temperature, $T_r$ is the room temperature and $T_m$ is the melting temperature of the material. The temperature change due to adiabatic heating is calculated as

$$\Delta T = \int_0^{\varepsilon_{eq}} \chi \frac{\sigma_{eq} d\varepsilon_{eq}}{\rho C_p} \tag{5}$$

where $\rho$ is the material density, $C_p$ is the specific heat and $\chi$ is the Taylor-Quinney coefficient that represents the proportion of plastic work converted into heat.

Failure is modelled using a criterion proposed by Cockcroft and Latham (CL) [27]

$$W = \int_0^{\varepsilon_{eq}} \langle \sigma_1 \rangle d\varepsilon_{eq} \leq W_c \tag{6}$$

where $\sigma_1$ is the major principal stress, $\langle \sigma_1 \rangle = \sigma_1$ when $\sigma_1 \geq 0$ and $\langle \sigma_1 \rangle = 0$ when $\sigma_1 < 0$. From Eq. (6) it is seen that failure cannot occur when there are no tensile stresses operating. The model constant $W_c$ is the value of $W$ at failure, and can be determined from a simple uniaxial tensile test. It was shown by e.g. Dey et al. [28] and Kane et al. [29] that the one-parameter CL criterion gives equally good results as more advanced failure criteria in simulations of perforation of steel plates under various stress states and projectile nose shapes. It should however be noted that owing to the anisotropic behaviour of the material and the uncertainty in the calibration of the CL criterion, $W_c$ should not be regarded as a material characteristic. In this study, the deviatoric stresses in the element are set to zero when $W$ reaches its critical value $W_c$ in a specified number of integration points. This is defined as material failure. However, the element continues to take compressive hydrostatic stresses until the time step size drops below a critical level. This is defined as element erosion. The constitutive relation and the failure criterion have been implemented in the non-linear explicit finite element codes IMPETUS Afea Solver [19] and LS-DYNA [30].

The bullet materials were modelled with the modified Johnson-Cook constitutive relation using the usual Johnson-Cook strain hardening law to describe the work hardening, while failure was described using the CL criterion. For more details regarding the modelling of the various bullet parts, see [1].

### *3.2. Identification of model parameters*

The yield stress $(A)$ and the hardening parameters $(Q_1, C_1, Q_2, C_2)$ were first fitted by a direct calibration to Bridgman-corrected true stress versus true plastic strain curves from the material tests in the rolling direction (Figure 3). These parameters were then used as initial values in LS-OPT [30], which is an optimization tool that interacts with LS-DYNA. An axisymmetric finite element model of the tensile specimen was created and several successive analyses were run in sequential order using a hybrid optimization algorithm with default values. Measured force-diameter reduction curves from the tensile tests in the rolling direction of the plates were used as response curves. Models with both coarse and fine element meshes were used in the optimization, but the difference in results was found to be minor. Optimized model parameters from the tensile tests in the rolling direction, together with mean-square-errors (MSE) from LS-OPT, are given in Table 5. The agreement between measured and fitted curves after optimization was excellent. This was also validated by running full 3D numerical simulations of the tensile tests using the IMPETUS Afea Solver and the material data in Table 5.

The rate sensitivity of high-strength aluminium alloys is usually found to be small at room temperature, and several experimental studies indicate an increase less than 10% from quasi-static loading conditions to a strain rate in the order of $10^3 \mathrm{s}^{-1}$ (see e.g. [16][31]). Owing to the lack of tensile test data at elevated strain rates and temperatures, the strain-rate sensitivity constant $c$ was given a small positive value [31], while $\dot{\varepsilon}_0$ was taken equal to the strain rate in the quasi-static tensile tests. It is thus assumed that the strain-rate sensitivity of the material is low and independent of temper. Further, the temperature sensitivity parameter $m$ was set to unity, implying a linear decrease in the flow stress with increasing temperature (as assumed for aluminium alloys in [32]). The fracture parameter $W_c$ was calibrated by use of the uniaxial tensile test in the rolling direction. In this case we simply have that $W_c = \int_0^{\varepsilon_f} \sigma d\varepsilon^p$. An alternative approach would have been to extract $W_c$ from the numerical simulations at the same diameter reduction as failure occurred in the experiments. This would give a somewhat higher value of $W_c$ compared to the value from the direct calibration. Note that the difference in $W_c$ with material direction is substantial (see Table 3). Since the stress level was not directionally dependent, the variation in $W_c$ reflects the anisotropy of the failure strain in uniaxial tension. This variation has not been taken into account in the simulations in

this study, but it was discussed in some detail in [16] for the anisotropic high-strength aluminium alloy AA7075-T651. Thus, only data from the tests in the rolling direction have been used in the calibration. Physical constants and model parameters common to all materials are provided in Table 6. The physical constants were given nominal values for aluminium alloys provided in the literature.

Constitutive relation, fracture criterion and model parameters for the different bullet materials were taken from Børvik et al. [1].

### *3.3. Finite element models*

All numerical simulations presented in the following were carried out using the explicit finite element code IMPETUS Afea Solver [19]. The projectile and the region in the target plate that undergo large plastic deformations were modelled using fully integrated 3rd-order 64-node hexahedrons. The target plate was modelled somewhat smaller ($80\times80\,\text{mm}^2$) than in the test to save computational time. Some analyses were also carried out with a full-size plate of $300\times300\,\text{mm}^2$, and the discrepancy in results compared to the reduced model was found to be negligible. The bulk of the simulations were done with only the rigid, hard steel core instead of the full bullet. This significantly reduced the CPU time without compromising the results too much, since it was shown experimentally in [14][15] that the brass jacket and the lead tip have a relatively small effect on the perforation process of monolithic 20 mm thick aluminium plates.

The symmetry in the problem was exploited by modelling only half the bullet and the plate. Outside the impact region 20 fully integrated linear elements with a node spacing of 1 mm in all directions were used, while 20 cubic 3rd-order 64-node elements were used over the thickness in the impact region. This gave a node spacing of 0.33 mm in all directions in the critical region. Plots of the 3D finite element meshes used in the bulk of the simulations are shown in Figure 10. Earlier studies have shown that perforation problems involving blunt projectiles causing shear localization are mesh-size sensitive, while the mesh-size dependency is less distinct for pointed nose projectiles causing failure by ductile hole growth (see e.g. [33][34]). To check the mesh-size dependency in the current problem, simulations were run on AA6070-O plates using respectively 7, 10, 20, 30, 40 and 50 cubic elements over the target thickness in the impact region. A constant impact velocity of $v_i = 550$ m/s was applied in these simulations. If less than 20 elements were used over the target thickness the mesh-size sensitivity was found to be strong, and the residual velocity increased by 20% when going

from 7 to 20 elements. However, a slight reduction in residual velocity of 4% was found when going from 20 to 50 elements over the target thickness. As a compromise between accuracy and CPU-time, 20 cubic elements were used over the target thickness in this study.

The constitutive behaviour of the target materials was modelled using the MJC relation with Voce hardening given by Eq. (4), while material failure was modelled using the CL failure criterion defined in Eq. (6). The bullet materials were modelled in a similar way as in Børvik et al. [1]. All simulations were run with the model parameters for the target plate based on the tensile tests in the rolling direction. When 16 of the 64 integration points in the higher-order elements reached failure, all deviatoric stresses were set to zero. However, the material was still allowed to take compressive hydrostatic stresses and failed elements were not eroded until their time step dropped below a user-defined critical level. In addition to failure caused by damage, the elements were also allowed to fail if the temperature reached the melting temperature of the material. Element erosion was used to prevent overly distorted elements which reduced the time step towards zero and could cause error termination. The critical time step for element erosion was set to 3 ns in this study.

Contact between the various parts was established using a penalty-based node-to-surface contact algorithm available in the IMPETUS Afea Solver. Friction between parts in contact was neglected since this will give a conservative estimate. In the current work, all exterior nodes and element faces were active in the contact. Free nodes of failed elements kept their mass and momentum, and remained active in the contact. Being given a physical radius to correctly represent the volume of eroded elements, free nodes were also in contact with each other.

### *3.4. Numerical results*

Typical simulations of the perforation process of a 20 mm thick AA6070 target plate in temper T6 impacted by the full bullet and by only the hard core of the bullet are shown in Figure 11 and Figure 12, respectively. Even though the mass of the full bullet is about twice as high as the core, the obtained difference in residual velocity is low. Thus, the experimental observation that the brass jacket and the lead tip only have a small effect on the perforation process was also captured in the numerical simulations.

Fringe and deformation plots of the perforation process for temper O and temper T4 at two different initial velocities are given in Figure 13, while similar plots for temper T6 and temper T7 are shown in Figure 14. The fringes represent the equivalent plastic strain. Also the

numerically obtained front-side and rear-side surfaces of the target plates after perforation are shown in the figures. Fragmentation has been found difficult to capture in numerical simulations [16], so only slight differences in physical behaviour between the various tempers are seen. These plots also reveal that only a small part of the target plate is affected by the highly localised perforation process, and hardly any global deformation is present. The area of the target plate with severe plastic strains is limited to a region with diameter just over two times the diameter of the projectile.

Regardless of the increased computational time of simulations applying the full APM2 bullet, a study was conducted to see if we could predict the deformation of the bullet and the stripping of the brass jacket during perforation. Analyses were conducted for all tempers at $v_i = 900$ m/s, and the numerical results were compared to post-perforation pictures taken from the high-speed videos. The results are presented in Figure 15, and it is seen that the deformation and stripping process are well captured. The brass jacket is completely removed from the steel core after perforation of plates in temper T4, T6 and T7, while it is still attached to the core after perforation of plates in temper O. This is consistent with the high-speed video images from the experiments.

Finally, the main results from a large number of simulations are presented as ballistic limit curves (i.e. curves of the residual versus initial velocity emanating from the ballistic limit of the target) in Figure 16, while predicted ballistic limit velocities are given in Table 4. The numerical predictions are found to be conservative, i.e. the ballistic limit velocities are under-estimated for all tempers. The numerical results exposed a maximum deviation in ballistic limit velocity from the experimental data of −17.2% for temper T7, and a minimum deviation of −13.5% for temper T4. Except for the fragmentation, the main trends observed in the tests were well captured in the simulations. All ballistic limit curves in Figure 16 have been obtained using the Recht-Ipson model in Eq. (3) with $a = 1$ and $p$ from the respective experimental data (Table 4).

## 4. Analytical method

### *4.1. CCET model*

Post-experimental inspections of the target plates indicated that the predominant failure mode during perforation is ductile hole growth (Figure 8 and Figure 9), although some

fragmentation was observed especially at the highest impact velocities. The high-speed videos of the ballistic experiments further suggested that the hard core of the APM2 bullet remained rigid throughout the perforation process (Figure 6 and Figure 7). Thus, the cylindrical cavity expansion theory (CCET) seems to be applicable for analytical modelling of the penetration and perforation process.

The CCET was first proposed by Bishop et al. [35] and further developed by Forrestal and co-authors (see e.g. [2]-[6]). Only a brief summary of the main equations as given by Forrestal and Warren [36] and Børvik et al. [14] will be presented in this study. To approximate ductile hole growth, the theory idealises the target as thin, independent layers that are compressed normal to the penetration direction [4]. Thus, the analysis is simplified to one-dimensional motion in the radial plate dimension for an elastic-plastic material. The cavity is then expanded from an initial radius of zero at a constant velocity $V$. This expansion produces both elastic and plastic responses. The elastic region has Young's modulus $E$ and Poisson's ratio $\nu$, while the plastic region is taken as an incompressible, power-law hardening material. Thus, the one-dimensional material response may be simplified as

$$\sigma = \begin{cases} E\varepsilon, & \sigma < \sigma_0 \\ \sigma_0 \left( \dfrac{E\varepsilon}{\sigma_0} \right)^n, & \sigma \geq \sigma_0 \end{cases} \tag{7}$$

where $\sigma$ is the true stress, $\varepsilon$ is the true strain, $\sigma_0$ is the yield stress and $n$ is the strain-hardening exponent. The model further requires the relation between the radial stress $\sigma_r$ at the cavity surface versus the cavity-expansion velocity $V$. It was shown in [4] that

$$\sigma_r = \sigma_s + \rho_t B V^2 \tag{8}$$

where $\sigma_s$ is the quasi-static radial stress required to open the cylindrical cavity, $\rho_t$ is the target density and $B$ is given as

$$B = \frac{1}{2} \left\{ \frac{1}{(1-\nu)\sqrt{1-\alpha^2}} \ln \left[ \frac{1+\sqrt{1-\alpha^2}}{\alpha} \right] + \gamma^2 - 2\ln[\gamma] - 1 \right\} \tag{9}$$

$$\alpha^2 = \frac{\sqrt{3}(1-2\nu)}{2(1-\nu)}\left(\frac{\rho_t V^2}{\sigma_0}\right) \quad \text{and} \quad \gamma^2 = \frac{2(1+\nu)\sigma_0}{\sqrt{3}E} \tag{10}$$

Assuming the von Mises yield criterion, $\sigma_s$ becomes

$$\sigma_s = \frac{\sigma_0}{\sqrt{3}}\left\{1+\left[\frac{E}{\sqrt{3}\sigma_0}\right]^n \int_0^b \frac{(-\ln x)^n}{1-x}\,dx\right\} \tag{11}$$

where $b = 1-\gamma^2$. As discussed in [37], the integral in Eq. (11) is improper due to the behaviour near $x = 0$. However, it has an integrable singularity at $x = 0$, and the integral can be numerically solved. Eq. (8) is then approximated by

$$\sigma_r = \sigma_s + \rho_t B_0 V^2 \tag{12}$$

where $B_0$ is a dimensionless constant obtained by curve-fitting to Eq. (8). This approximation is required to obtain closed-form perforation equations because $B$ is a function of $V$.

Closed-form perforation equations for rigid projectiles during impact of the target plate can now be established. For an ogival-nose projectile with mass $m_p$ and impact velocity $v_i$, the ballistic limit velocity $v_{bl}$ and the residual velocity $v_r$ are expressed by [36]

$$v_{bl} = \left(\frac{2\sigma_s}{\rho_p}\frac{h}{(L+k_1 l)}\right)^{1/2}\left[1+C+\frac{2}{3}C^2\right]^{1/2} \tag{13}$$

$$v_r = v_{bl}\left[\left(\frac{v_i}{v_{bl}}\right)^2 - 1\right]^{1/2}\left[1-C+\frac{1}{2}C^2\right] \tag{14}$$

$$C = \frac{h}{(L+k_1 l)}\frac{\rho_t}{\rho_p}B_0 N(\psi) \tag{15}$$

$$N(\psi) = 8\psi^2 \ln\left(\frac{2\psi}{2\psi-1}\right) - (1+4\psi) \tag{16}$$

$$m_p = \pi \rho_p a^2 \left( L + k_1 l \right) \tag{17}$$

$$k_1 = \left( 4\psi^2 - 4\psi/3 + 1/3 \right) - \frac{4\psi^2 \left( 2\psi - 1 \right)}{\sqrt{4\psi - 1}} \sin^{-1} \left[ \frac{\sqrt{4\psi - 1}}{2\psi} \right] \tag{18}$$

$$\psi = \frac{1}{4} \left[ \left( \frac{l}{a} \right)^2 + 1 \right] \tag{19}$$

In the equations given above, the ogival-nose projectile has mass $m_p$, density $\rho_p$, shank length $L$, nose length $l$, diameter $2a$ and caliber-radius-head $\psi$. The target plate has density $\rho_t$, thickness $h$, $\sigma_s$ is given by Eq. (11) and $B_0$ is found by fitting Eq. (12) to Eq. (8). If the value of $C$ in Eq. (15) is small compared to unity, Eqs. (13) and (14) can be reduced to

$$v_{bl} = \left( \frac{2\sigma_s}{\rho_p} \frac{h}{\left( L + k_1 l \right)} \right)^{1/2} \tag{20}$$

$$v_r = v_{bl} \left[ \left( \frac{v_i}{v_{bl}} \right)^2 - 1 \right]^{1/2} \tag{21}$$

where Eq. (21) is identical to the Recht-Ipson model [22] for pointed-nose projectiles (i.e. $a = 1$ and $p = 2$). Note that Eq. (6) in [14], which is equivalent to Eq. (14) given above, has a misprint: the last term with $C$ should be to the power of 1 and not ½.

### *4.2. CCET calculations*

All equations needed for CCET calculations of the perforation problem are given above. First, since the simplified constitutive relation used in the CCET calculations differs from the one used in the finite element simulations, a new calibration was required. This was done by a direct curve fit of Eq. (7) to the Bridgman-corrected true stress versus true plastic strain curves from the material tests in the rolling direction for the various tempers. Then, the values of $B_0$ were obtained by conducting curve fits of Eq. (12) to Eq. (8) using a MATLAB script.

In the CCET calculations, only the hard core of the APM2 bullet was considered. Since the shank of the core in Figure 4 is truncated towards the brass sabot, an equivalent shank length $L$ and an equivalent nose length $l$ were calculated from Eqs. (17)−(19) that match the measured mass of the core. With $m_p = 5.25\,\text{g}$, $\rho_p = 7850\,\text{kg/m}^3$, $2a = 6.17\,\text{mm}$ and $\psi = 3$, we find $L = 16.8\,\text{mm}$ and $l = 10.2\,\text{mm}$. Now the value of $C$ in Eq. (15) can be calculated (or assumed negligible, i.e. $C$ is equal to zero), and the ballistic limit velocities and the ballistic limit curves can be predicted from Eqs. (13) and (14).

Results from the CCET calculations are given in Table 7, while predicted ballistic limit curves based on Eq. (14) are compared to the corresponding experimental curves in Figure 17. The predicted ballistic limits are in general in good agreement with the experimental data, especially for $C$ equal to zero, and in much better agreement with the experimental data than the ballistic limits based on finite element simulations for all tempers. This is rather interesting taking the simplicity of the closed-form equations compared to the more advanced finite element models into account. However, in contrast to the FE simulations most CCET calculations predict non-conservative results, i.e. the predicted ballistic limit velocity is slightly higher than the corresponding experimental result.

## 5. Discussion and conclusions

In this paper, the ballistic properties of the aluminium alloy AA6070 in four different tempers (O, T4, T6 and T7) have been studied. The various heat treatments give significant changes in the mechanical properties of the alloy, while keeping the grain structure unaltered. Based on a number of quasi-static tensile tests on smooth axisymmetric specimens in three different in-plane directions it was found that the anisotropy of the material in flow stress is negligible, while the anisotropy in strain to failure is significant. Temper T6 was found to have the highest yield stress and the lowest ductility, while the opposite was found for temper O. Temper T4 and T7 were in-between these two extremes, but the strain hardening in the former was considerably stronger than for the other tempers.

Ballistic impact tests using 7.62 mm APM2 bullets with a hardened steel core were carried out, and the ballistic limit velocity for each temper of 20 mm thick plates of AA6070 was determined. In a similar way as for thin steel plates impacted by the same bullet, a marked increase in perforation resistance with target yield stress was found. This increase in

perforation resistance seems to be independent of the local ductility of the alloy. Post-experimental investigations of the target plates confirmed that ductile hole growth was the predominant fracture mode, even though fragmentation from both sides of the target plate occurred at the highest impact velocities. However, as the impact velocity of the bullet approached the ballistic limit velocity the degree of fragmentation was considerably reduced, which indicates that the fragmentation process has limited effect on the protection level of the relatively thick target plates used in this study.

A thermoelastic-thermoviscoplastic constitutive relation and a ductile fracture criterion were calibrated based on the material tests, and applied in 3D numerical simulations using the IMPETUS Afea Solver with fully integrated higher-order hexahedrons. Both the full bullet and only the hard core of the bullet were used in simulations, and the results confirmed the experimental observation that the brass jacket and the lead tip have little effect on the perforation process. Thus, only the hard steel core of the bullet was used in the prediction of the ballistic limit velocities. All numerical results were found to be conservative with respect to the experimentally obtained ballistic limit velocity. Analytical calculations using the cylindrical cavity expansion theory were also carried out. Even though effects like strain rate hardening and temperature softening were neglected in the CCET calculations, excellent agreement with the experimental data was obtained for all tempers. The CCET calculations were also found to be in better agreement with the experimental data than the FE simulations.

There may be several reasons for the under-estimation of the ballistic limit velocity in the numerical simulations, such as the element size of the higher-order hexahedrons in the impact region, a too simple representation of the constitutive behaviour and/or the fracture process, the accuracy of the mathematical models and algorithms, or uncertainties in the applied model parameters (see also the discussions in [16], [17] and [38]). Figure 18 shows a comparison of the ballistic limit velocities for the four different tempers of AA6070 based on experimental tests, numerical simulations and CCET calculations. The experimental data and the CCET results are virtually on top of each other, while the numerical predictions show an almost constant offset. Thus, the experimental trend is well predicted by the numerical simulations. It was concluded in [33] that the main reason for the difference between CCET and FEM is the lack of material softening due to thermal effects in the former. It was also shown that if temperature softening is introduced in CCET, or omitted in FEM, the two methods give similar results. Note that a tiny pinhole in the plate was used to avoid the need for a fracture criterion in [33]. Also in the current study it is believed that the difference in results between CCET and FEM is related to the thermal softening of the material. New FEM simulations

were run assuming isothermal conditions and the ballistic limit was found to increase by 5-10%. In addition, the rate-sensitivity of the aluminium alloy was assumed low and independent of temper in this study. It is however well known that at elevated temperatures the strain-rate sensitivity may be considerably increased. This may also have contributed to the conservative predictions. Another reason for the discrepancy between CCET and FEM is erosion of the rather coarse cubic elements. As indicated by the mesh-size sensitivity study presented in Section 3.3, a refined mesh will give a slight increase in ballistic limit velocity. Cubic elements are more bulky than linear elements if the number of nodes over the target thickness is constant, and when eroded too much material in the impact zone may be lost.

It is of interest to compare the results from this research with data from similar studies on other materials under ballistic impact by 7.62 mm APM2 bullets. Table 8 gives a collection of material data and experimentally obtained ballistic limit velocities for a number of materials tested under identical impact conditions. For the aluminium plates $v_{bl}$ is based on 20 mm thick plates, while for the steel plates $v_{bl}$ is based on 12 mm thick plates. The material data stem from uniaxial tensile tests at quasi-static strain rate and room temperature on smooth, axisymmetric specimens taken in the rolling direction of the plate. Further, the ballistic limit velocities $v_{bl}$ and the kinetic energy at the ballistic limit $E_{bl} = \frac{1}{2} m_p v_{bl}^2$ (where $m_p$ is the full bullet mass) are divided by the areal mass $m_A$ to highlight the perforation resistance and the energy absorption per unit mass. From this table, two important observations are done. Firstly, the ballistic limit velocity is an increasing function of the yield stress, independent of target material, local ductility and plastic work to failure. The only exception is the AA6070-T4, but this temper has a strong strain hardening compared to the other tempers, as shown in Figure 3. Secondly, the values of the ballistic limit velocity divided by the areal mass (i.e. $v_{bl} / m_A$) obtained for several of the aluminium alloys (especially the AA7075-T651) are superior to those of the toughest armour steels. However, the kinetic energy at the ballistic limit divided by the areal mass $m_A$ is slightly higher for the armour steels than for the high-strength aluminium. These results strongly suggest that high-strength aluminium alloys have comparable perforation resistance to high-strength steels when areal mass is taken into account. It should finally be mentioned that a scale effect may be present since the tested aluminium plates are considerably thicker than the steel plates. Since the targets have been impacted by real bullets fired from a real weapon, this is of less importance in design.

**Acknowledgement**

The financial support of this work from the Structural Impact Laboratory (SIMLab), Centre for Research-based Innovation (CRI) at the Norwegian University of Science and Technology, is gratefully acknowledged. The authors also would like to express their gratitude to Dr. Michael J. Forrestal and Dr. Tom L. Warren for fruitful discussions regarding the cavity expansion theory.

**References**

[1] Børvik T, Dey S, Clausen AH. Perforation resistance of five different high-strength steel plates subjected to small-arms projectiles. International Journal of Impact Engineering 2009;36:948-964.
[2] Forrestal MJ, Rosenberg Z, Luk VK, Bless SJ. Perforations of aluminum plates with conical-nosed projectiles. Journal of Applied Mechanics 1987; 54: 230-232.
[3] Rosenberg Z, Forrestal MJ. Perforations of aluminum plates with conical-nosed rods-Additional data and discussion. Journal of Applied Mechanics 1988; 55: 236-238.
[4] Forrestal MJ, Luk VK, Brar NS. Perforation of aluminum armor plates with conical-nose projectiles. Mechanics of Materials 1990;10:97-105
[5] Forrestal MJ, Luk VK, Rosenberg Z, Brar NS. Penetration of 7075-T651 aluminum targets with ogival-nose projectiles. International Journal of Solids and Structures 1992;29:1729-36.
[6] Piekutowski AJ, Forrestal MJ, Poormon KL, Warren TL. Perforation of aluminum plates with ogive-nose steel rods at normal and oblique impacts. International Journal of Impact Engineering 1996;18:877-887.
[7] Anderson Jr CE, Dannemann KA. Deformation and damage of two aluminium alloys from ballistic impact. In: Furnish M, Thadhani NN, Horie Y, editors. Shock compression of condensed matter-2001, vol 620. Melville, NY: American Institute of Physics; 2002. p. 1298–301.
[8] Gooch WA, Burkins MS, Squillacioti RJ. Ballistic testing of commercial aluminium alloys and alternative processing techniques to increase the availability of aluminum armor. Proceedings of the 23rd International Symposium on Ballistics, Spain, 2007.
[9] Cheeseman A, Gooch WA, Burkins MS. Ballistic evaluation of aluminum 2139-T8. In: Bless SJ, Walker JW, (Eds.), Proceedings of the 24th International Symposium on Ballistics, September 2008, New Orleans, USA, p. 651.
[10] Demir T, Ubeyli M, Yildirim RO. Investigation on the ballistic impact behaviour of various alloys against 7.62 mm armor piercing projectile. Mater Des 2008;29:2009–16.
[11] Iqbal MA, Chakrabarti A, Beniwal S, Gupta NK. 3D numerical simulations of sharp nosed projectile impact on ductile targets. International Journal of Impact Engineering 2010;37:185-195.
[12] Sullivan A, Derry C, Robson JD, Horsfall I, Prangnell PB. Microstructure simulation and ballistic behaviour of weld zones in friction stir welds in high strength aluminium 7xxx plate. Materials Science and Engineering A 2011;528:3409-3422.
[13] Jones N, Paik JK. Impact perforation of aluminium alloy plates. International journal of Impact Engineering 2012;48:46-53.

[14] Børvik T, Forrestal MJ, Warren TL. Perforation of 5083-H116 aluminum armor plates with ogive-nose rods and 7.62 mm APM2 bullets. Experimental Mechanics 2010;50:969-978.
[15] Forrestal MJ, Børvik T, Warren TL. Perforation of 7075-T651 Aluminum Armor Plates with 7.62mm APM2 Bullets. Experimental Mechanics 2010;50:1245-1251.
[16] Børvik T, Hopperstad OS, Pedersen KO. Quasi-brittle fracture during structural impact of AA7075-T651 aluminium plates. International Journal of Impact Engineering 2010;37:537-551.
[17] Pedersen KO, Børvik T, Hopperstad OS. Fracture mechanisms of aluminium alloy AA7075-T651 under various loading conditions. Materials & Design 2011;32:97-107.
[18] Hatch JE. Aluminium: Properties and Physical Metallurgy. American Society for Metals, Metals Park, Ohio, 1984.
[19] http://www.impetus.no [cited: 26.09.2012].
[20] Børvik T, Langseth M, Hopperstad OS, Malo KA. Ballistic penetration of steel plates. International Journal of Impact Engineering 1999;22:855–87.
[21] Børvik T, Hopperstad OS, Langseth M, Malo KA. Effect of target thickness in blunt projectile penetration of Weldox 460 E steel plates. International Journal of Impact Engineering 2003;28(4):413-464.
[22] Recht RF, Ipson TW. Ballistic perforation dynamics. Journal of Applied Mechanics 1963;30:384-390.
[23] Goldsmith W. Non-ideal projectile impact on targets. International Journal of Impact Engineering 1999;22:95–395.
[24] Børvik T, Hopperstad OS, Berstad T, Langseth M. A computational model of viscoplasticity and ductile damage for impact and penetration. European Journal of Mechanics – A/Solids 2001;5:685-712.
[25] Wadley HNG, Børvik T, Olovsson L, Wetzel JJ, Dharmasena KP, Hopperstad OS, Deshpande VS, Hutchinson JW. Deformation and fracture of impulsively loaded sandwich panels. In press, Journal of the Mechanics and Physics of Solids 2012 (http://dx.doi.org/10.1016/j.jmps.2012.07.007).
[26] Lemaitre J, Chaboche J-L. Mechanics of solid materials. Cambridge University Press, Cambridge, 1990.
[27] Cockcroft MG, Latham DJ. Ductility and workability of metals. Journal Institute of Metals 1968;96:33-39.
[28] Dey S, Børvik T, Hopperstad OS, Langseth M. On the influence of fracture criterion in projectile impact of steel plates. Computational Materials Science 2006;38:176-191.
[29] Kane A, Børvik T, Berstad T, Hopperstad OS. Failure criteria with unilateral conditions for simulation of plate perforation. European Journal of Mechanics – A/Solids 2011;30:468-476.
[30] http://www.lstc.com [cited: 26.09.2012]
[31] Oosterkamp LD, Ivankovic A, Venizelos G. High strain rate properties of selected aluminium alloys. Materials Science and Engineering A 2000;278:225-235.
[32] Johnson G. Material characterization for warhead computations. In: Tactical Missile Warheads, Edited by J. Carleone, Progress in Astronautics and Aeronautics, Volume 155, 1993, American Institute of Aeronautics and Astronautics, Washington.
[33] Børvik T, Forrestal MJ, Hopperstad OS, Warren T, Langseth M. Perforation of AA5083-H116 aluminium plates with conical-nose steel projectiles – calculations. International Journal of Impact Engineering 2009;36(3):426–437.
[34] Børvik T, Olovsson L, Dey S, Langseth M. Normal and oblique impact of small arms bullets on AA6082-T4 aluminium protective plates. International Journal of Impact Engineering 2011;38:577-589.

[35] Bishop RF, Hill R, Mott NF. The theory of indentation and hardness. Proceedings of the Royal Society 1945;57:147-159.
[36] Forrestal MJ, Warren TL. Perforation equations for conical and ogival nose rigid projectiles into aluminum target plates. International Journal of Impact Engineering 2009;36:220-225.
[37] Forrestal MJ, Romero LA. Comment on 'Perforation of Aluminum Plates with Ogive-nose Steel Rods at Normal and Oblique Impacts' (Int J Impact Eng 1996;18:877-887). International Journal of Impact Engineering 2007;34:1962-1964.
[38] Zukas JA. Introduction to hydrocodes. Studies in Applied Mechanics 2004;49:1-313.
[39] Lou DC, Solberg JK, Børvik T. Surface strengthening using a self-protective diffusion paste and its application for ballistic protection of steel plates. Material & Design 2009;30:3525-3536.

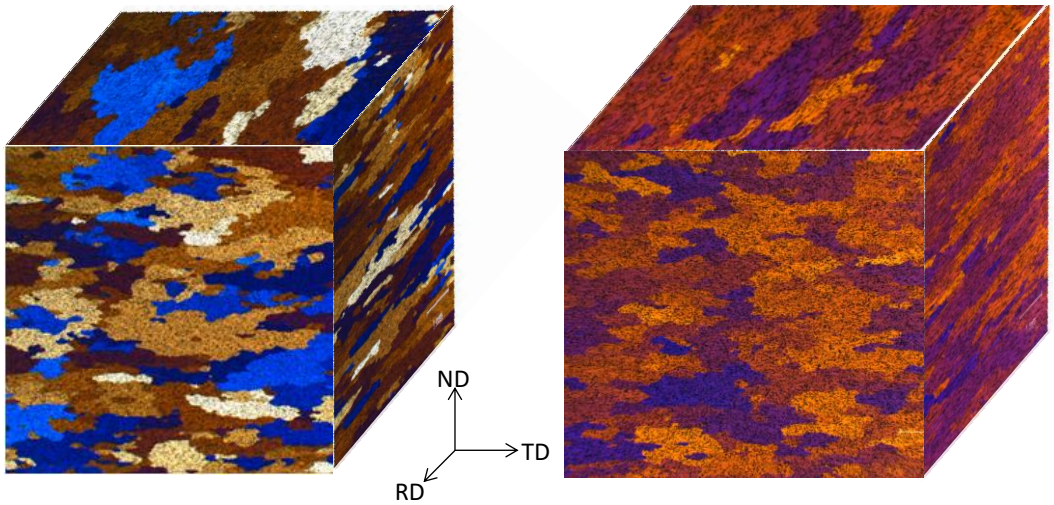


(a) AA6070-O (b) AA6070-T6

Figure 1. Tri-planar optical micrographs showing the grain structure after heat treatments to temper a) O and b) T6 for the aluminium alloy AA6070, where RD gives the rolling direction, TD gives the transverse direction and ND gives the normal direction of the plate.

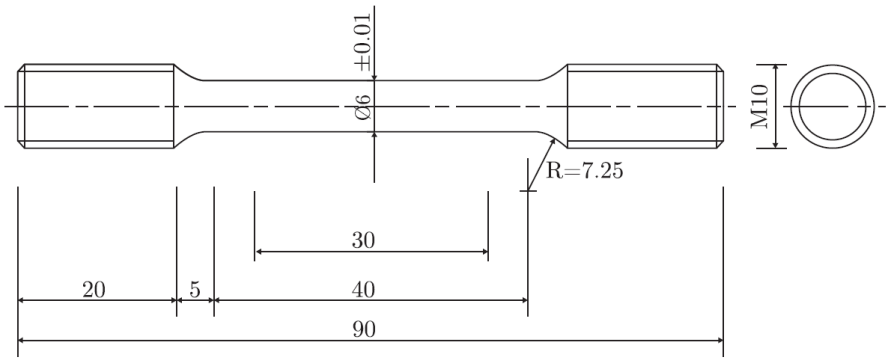


Figure 2. Geometry of the tensile specimen (dimensions in mm).

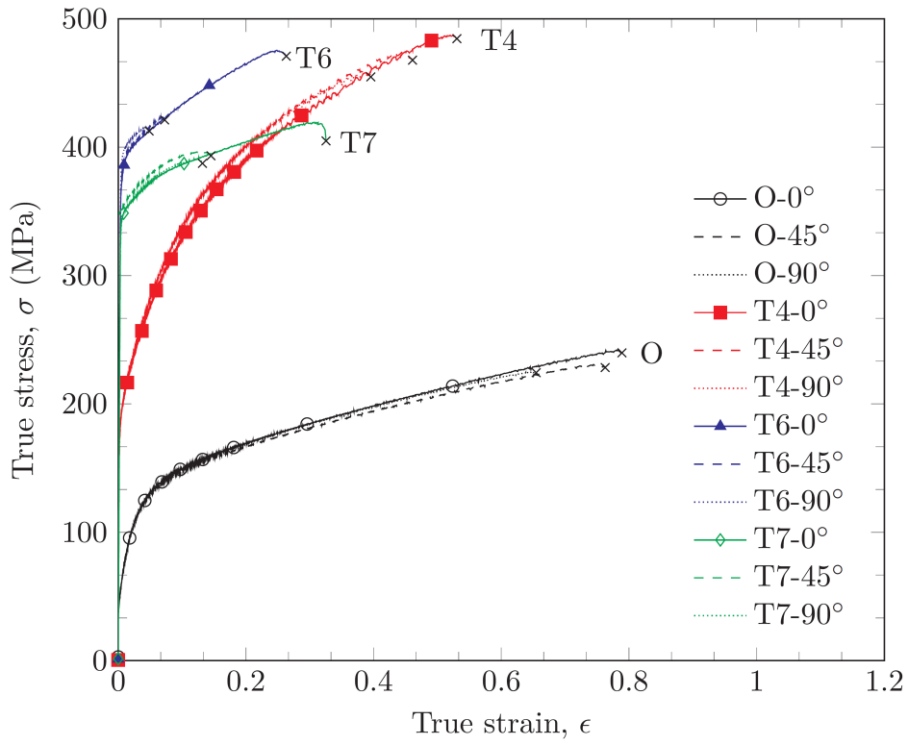


Figure 3. Typical true stress-strain curves of all tempers and test orientations (where the black ×'s indicate the fracture strain).

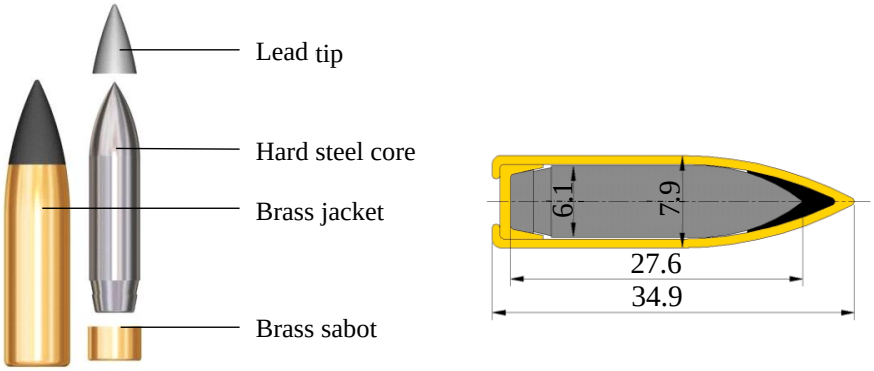


Figure 4. Schematic drawings and geometry of the 7.62 mm bullet (dimensions in mm).

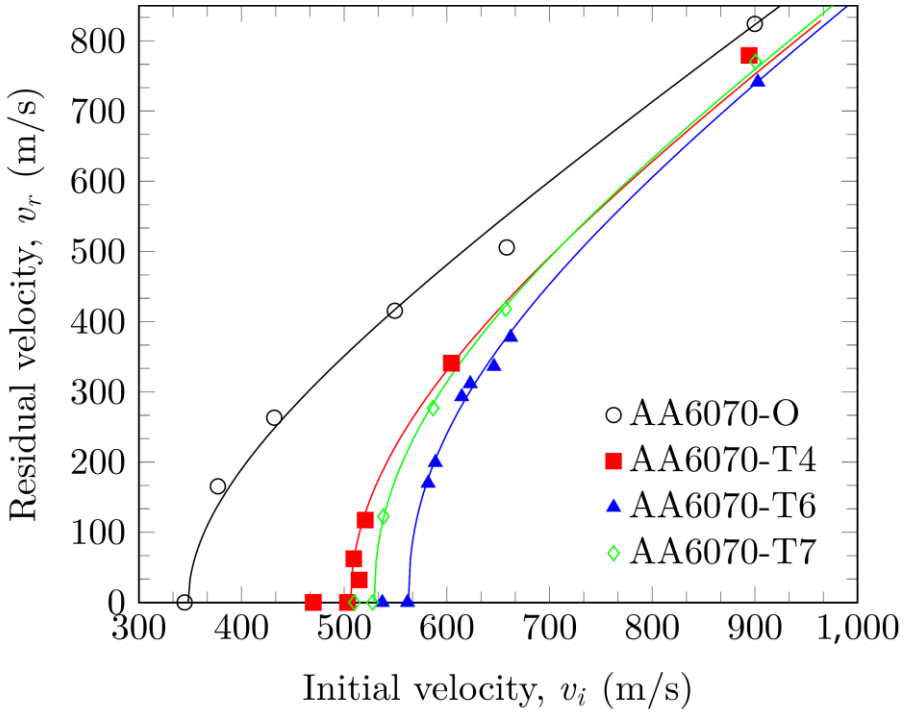


Figure 5. Ballistic limit curves for the four different tempers of AA6070.

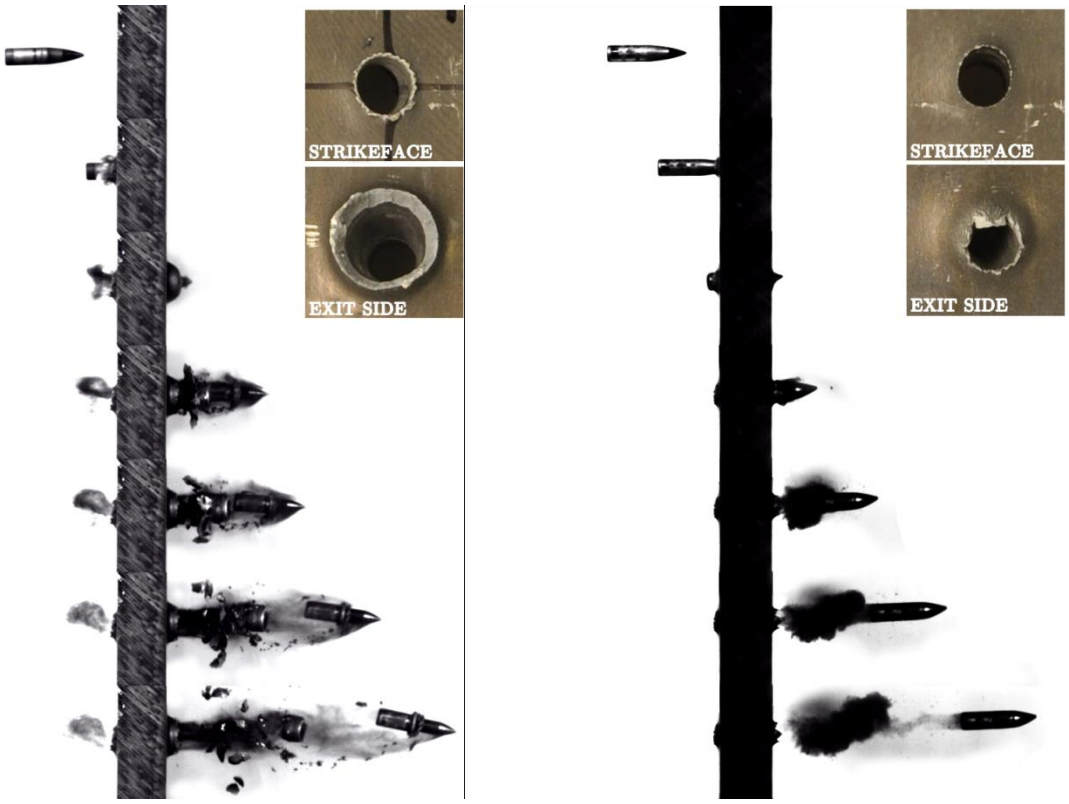


(a) $v_i = 900$ m/s and $v_r = 824$ m/s (b) $v_i = 377$ m/s and $v_r = 165$ m/s

Figure 6. High-speed video images showing the perforation process of a 20 mm thick AA6070 plate in temper O impacted by the APM2 bullet at two different velocities.

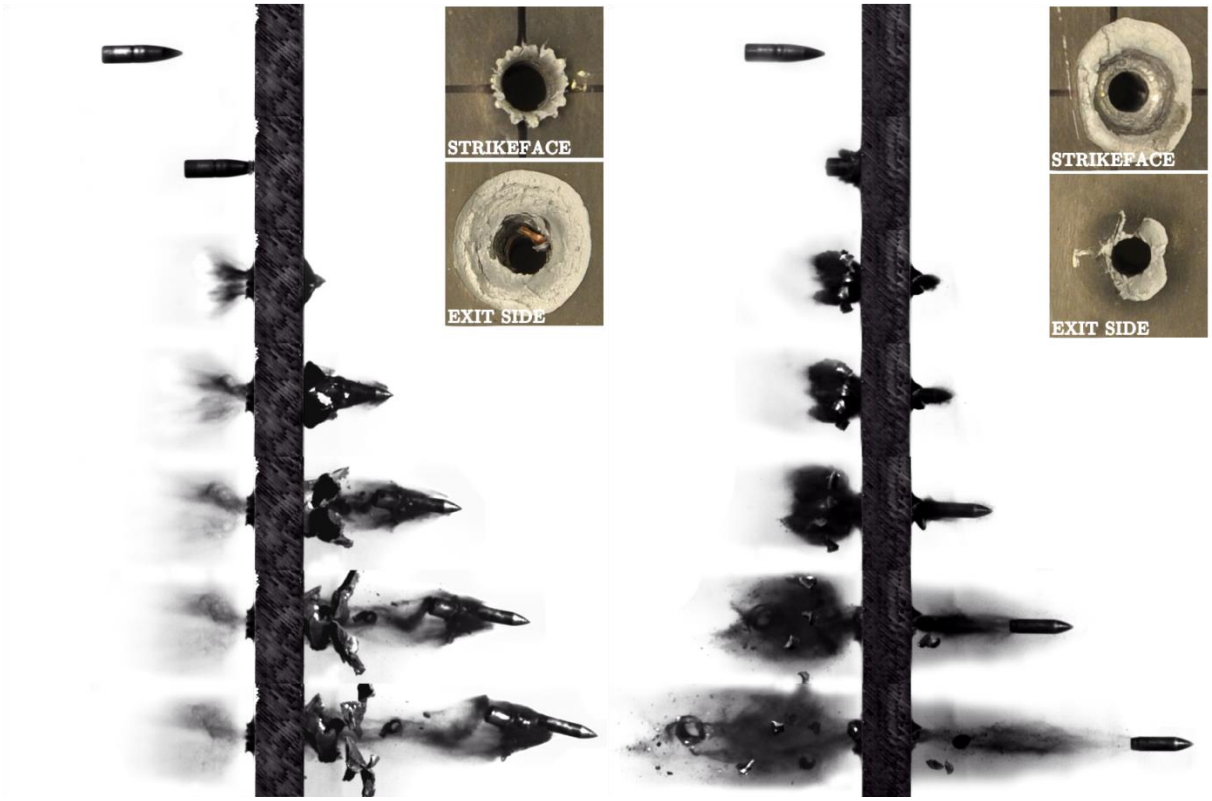


(a) $v_i = 903$ m/s and $v_r = 741$ m/s (b) $v_i = 615$ m/s and $v_r = 293$ m/s

Figure 7. High-speed video images showing the perforation process of a 20 mm thick AA6070 plate in temper T6 impacted by the APM2 bullet at two different velocities.

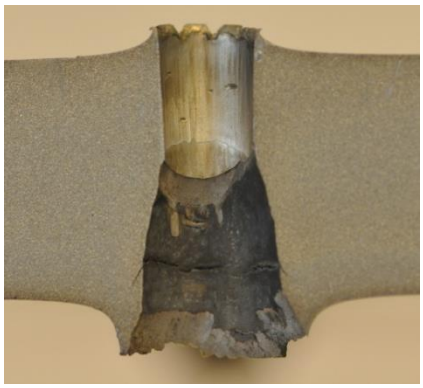

(a) $v_i = 900$ m/s and $v_r = 824$ m/s

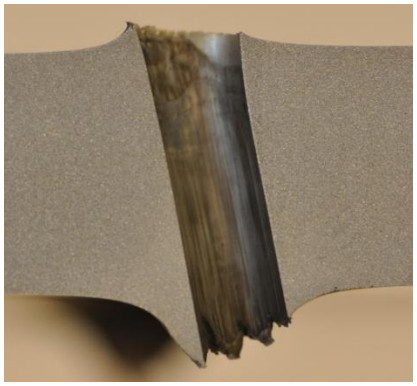

(b) $v_i = 377$ m/s and $v_r = 165$ m/s

Figure 8. Pictures of cross-sections of 20 mm thick target plates of AA6070 in temper O perforated by APM2 bullets at various impact velocities.

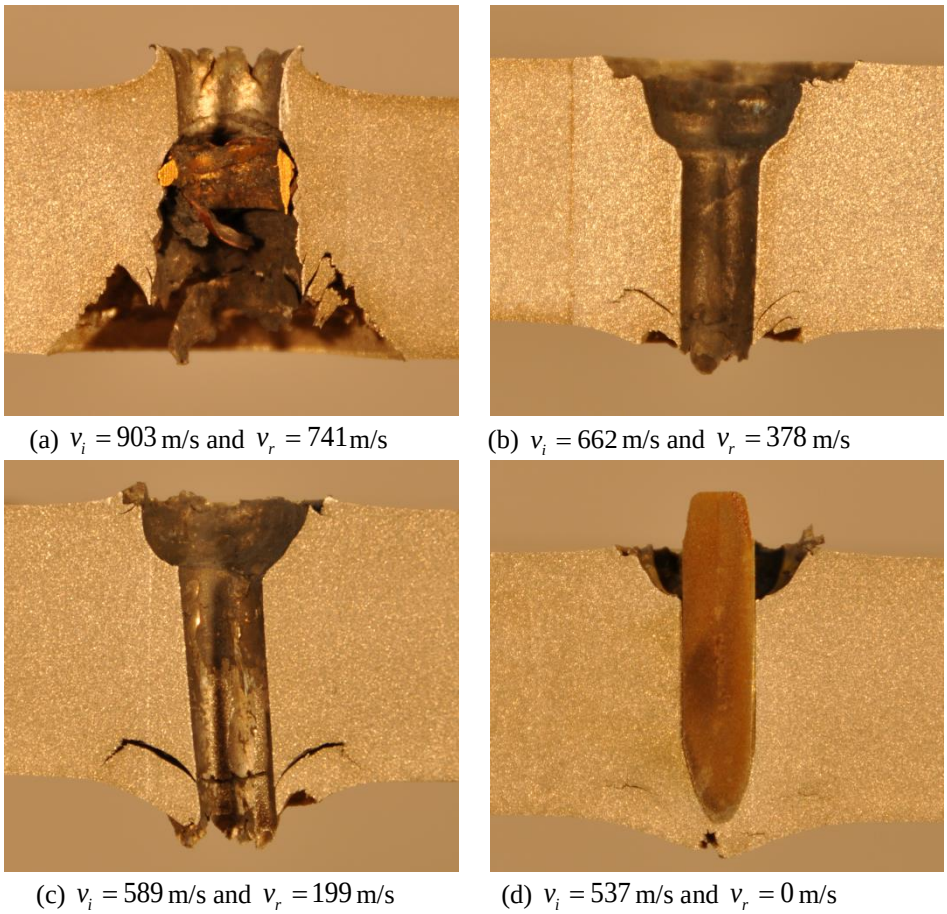

(a) $v_i = 903$ m/s and $v_r = 741$ m/s (b) $v_i = 662$ m/s and $v_r = 378$ m/s

(c) $v_i = 589$ m/s and $v_r = 199$ m/s (d) $v_i = 537$ m/s and $v_r = 0$ m/s

Figure 9. Pictures of cross-sections of 20 mm thick target plates of AA6070 in temper T6 perforated by APM2 bullets at various impact velocities.

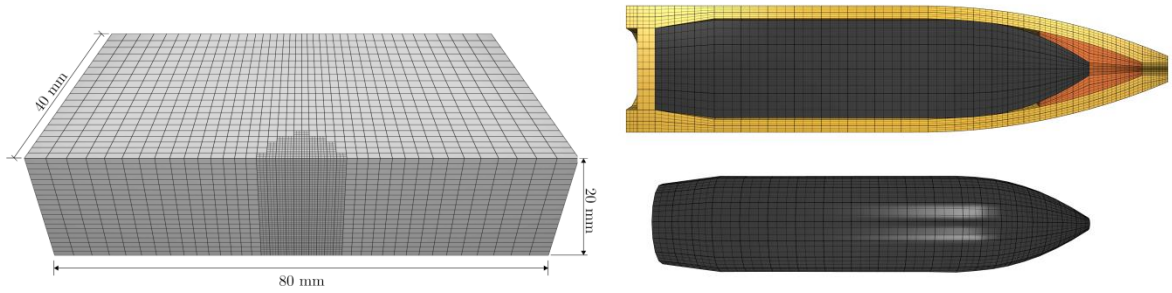


(a) (b)

Figure 10. 3D solid element meshes used in the numerical simulations: (a) aluminium plate with 8-node linear elements in the periphery and 64-node cubic elements in the impact area (two times the radius of the bullet), and (b) APM2 bullet with 64-node cubic elements.

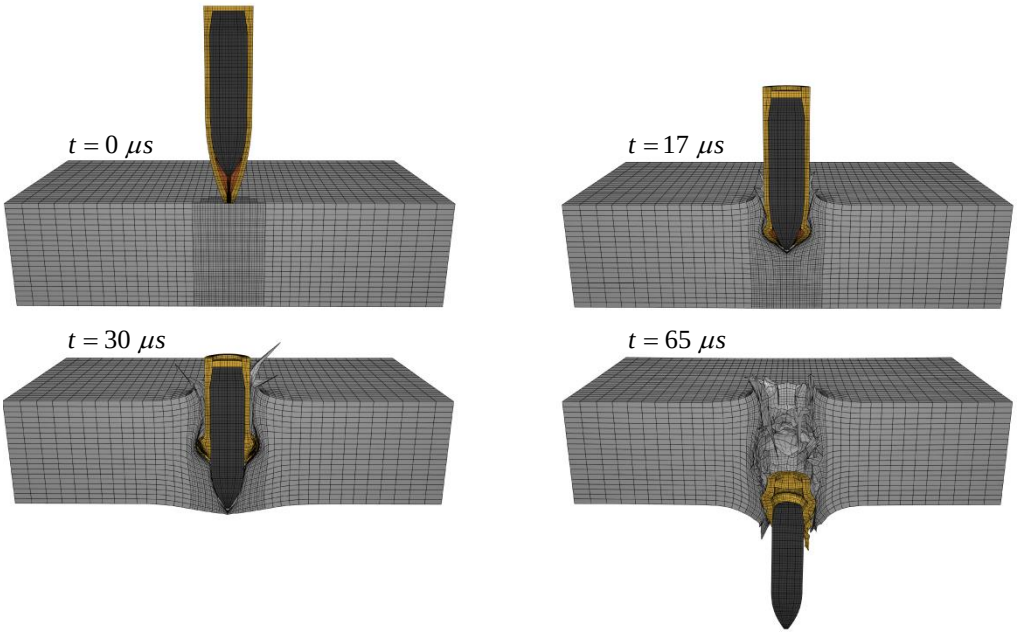


Figure 11. Perforation process (where $t$ provides the time after impact) of a 20 mm thick AA6070 plate in temper T6 by the full APM2 bullet with impact velocity $v_i = 903$ m/s and residual velocity $v_r = 784$ m/s .

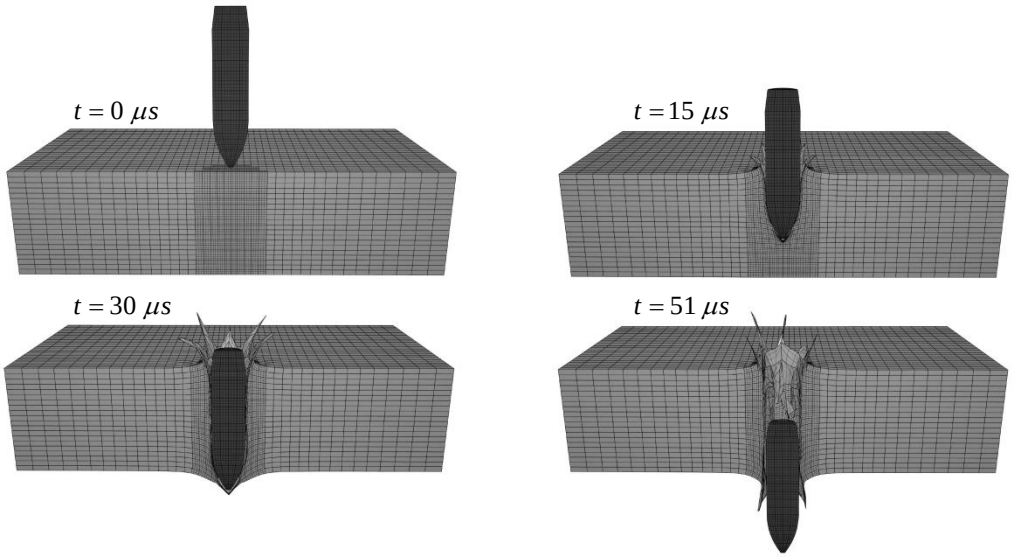


Figure 12. Perforation process (where $t$ provides the time after impact) of 20 mm thick AA6070 plate in temper T6 by only the hard core of the APM2 bullet with impact velocity $v_i = 903$ m/s and residual velocity $v_r = 754$ m/s .

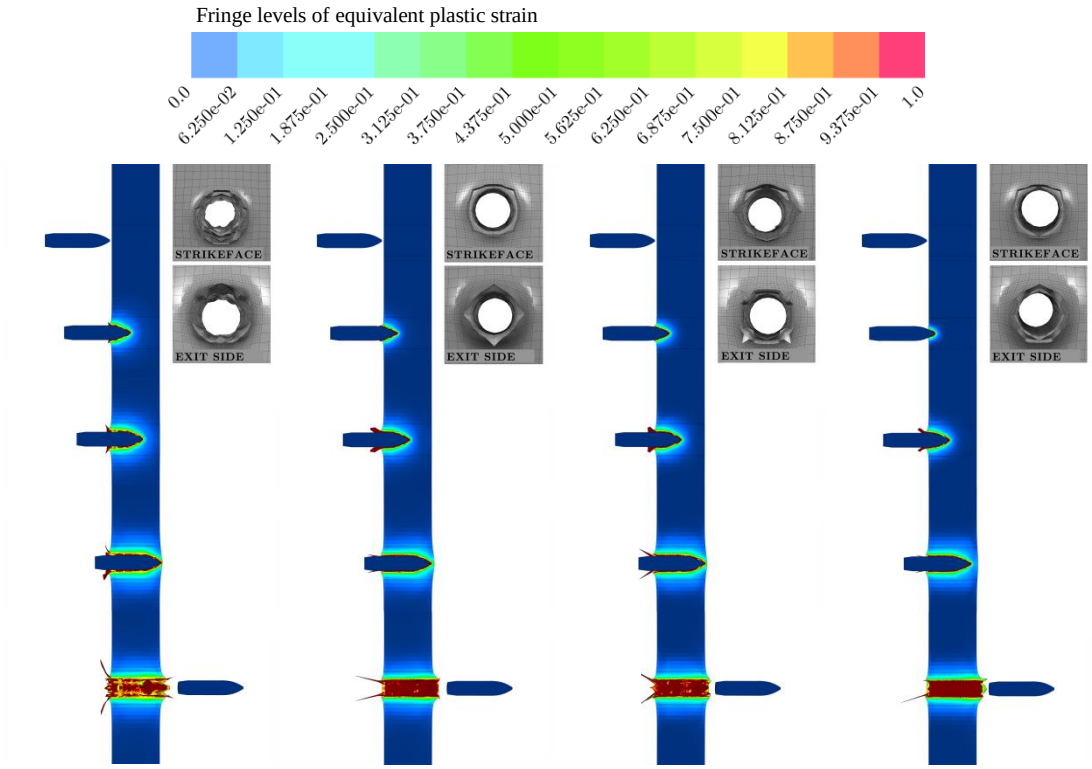


Figure 13. Plots of the perforation process of 20 mm thick AA6070 plate at two different impact velocities: (a) O-temper with $v_i = 900$ m/s and $v_r = 834$ m/s, (b) O-temper with $v_i = 377$ m/s and $v_r = 231$ m/s, (c) T4-temper with $v_i = 894$ m/s and $v_i = 769$ m/s, (d) T4-temper with $v_i = 509$ m/s and $v_i = 266$ m/s. The fringes show the equivalent plastic strain.

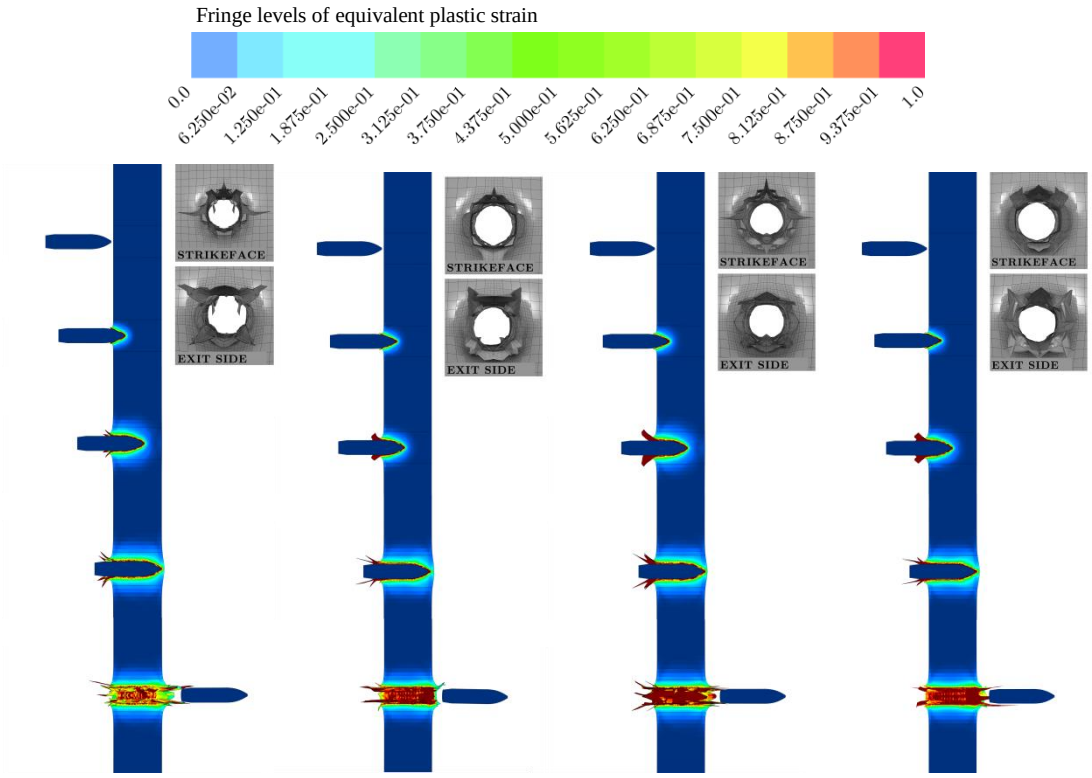


Figure 14. Plots of the perforation process of 20 mm thick AA6070 plate at two different impact velocities: (a) T6-temper with $v_i = 903\,\text{m/s}$ and $v_r = 754\,\text{m/s}$, (b) T6-temper with $v_i = 615\,\text{m/s}$ and $v_r = 395\,\text{m/s}$, (c) T7-temper with $v_i = 901\,\text{m/s}$ and $v_i = 764\,\text{m/s}$, (d) T7-temper with $v_i = 538\,\text{m/s}$ and $v_i = 374\,\text{m/s}$. The fringes show the equivalent plastic strain.

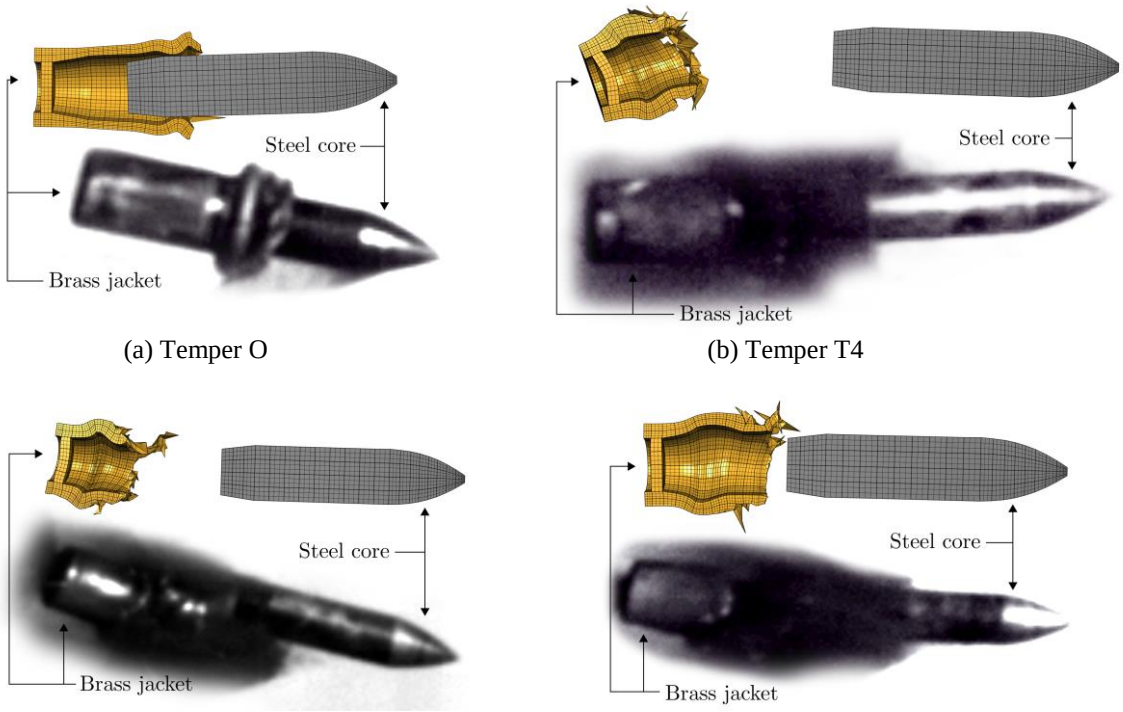


(a) Temper O (b) Temper T4

(c) Temper T6 (d) Temper T7

Figure 15. Comparison of APM2 bullets after perforation in tests and simulations. All pictures and predictions are from the maximum velocity tests ( $v_i \approx 900$ m/s ).

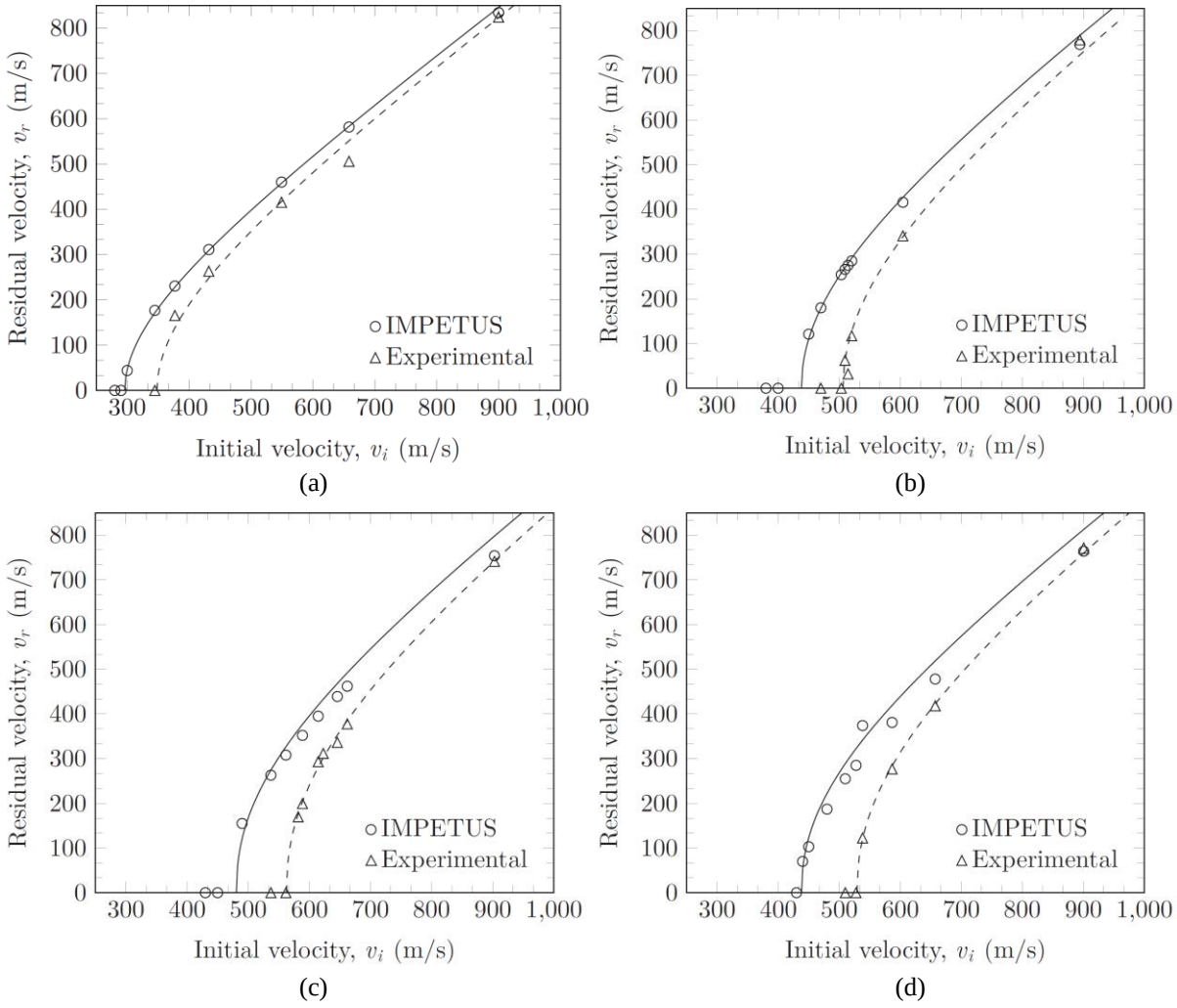


Figure 16. Predicted ballistic limit curve for (a) AA6070-O, (b) AA6070-T4, (c) AA6070-T6 and (d) AA6070-T7 from the numerical simulations compared to the experimental curve.

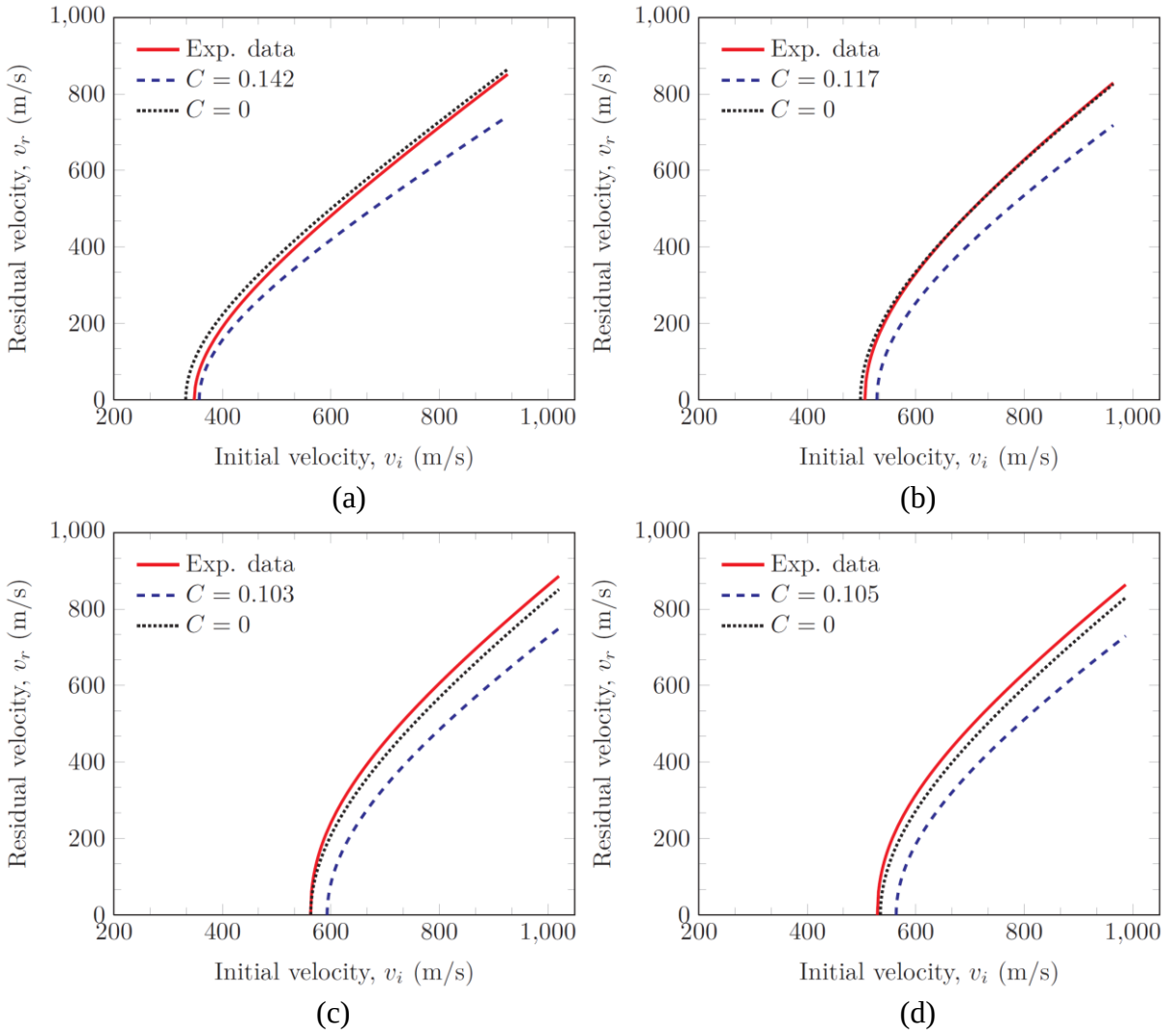


Figure 17. Predicted ballistic limit curves for (a) AA6070-O, (b) AA6070-T4, (c) AA6070-T6, and (d) AA6070-T7 impacted by 7.62 mm APM2 bullets from CCET calculations (using two different values of $C$) compared to the experimental curve.

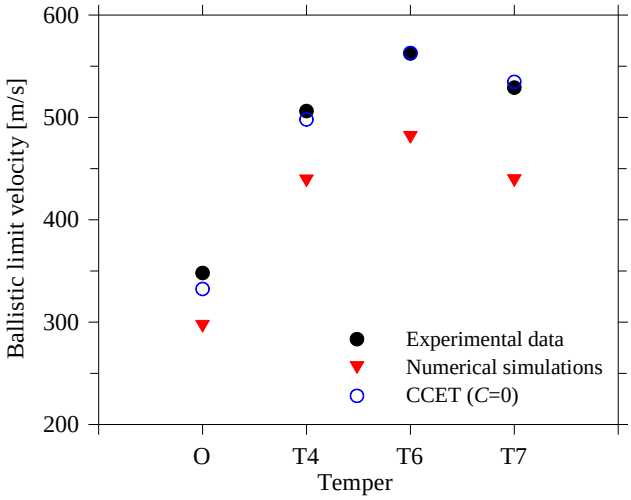


Figure 18. Comparison of ballistic limit velocities for the four different tempers of AA6070 from experimental tests, numerical simulations and CCET calculations.

Table 1. Chemical components (in weight %) of aluminium alloy AA6070.

| Al | Si | Fe | Cu | Mn | Mg | Others |
|---|---|---|---|---|---|---|
| Balance | 1.38 | 0.22 | 0.26 | 0.54 | 1.23 | 0.15 |

Table 2. Heat treatment processes of AA6070 to obtain the different tempers.

| Temper | Solutionizing | Cooling | Annealing/artificial aging | Cooling |
|---|---|---|---|---|
| O | 90 min at 560 °C (+5 °C) | Water quench | 24 h at 350 °C (+5 °C) | Slow cooling |
| T4 | 90 min at 560 °C (+5 °C) | Water quench | — | — |
| T6 | 90 min at 560 °C (+5 °C) | Water quench | 64 h at 160 °C (+5 °C) | Slow cooling |
| T7 | 90 min at 560 °C (+5 °C) | Water quench | 8 h at 200 °C (+5 °C) | Slow cooling |

Table 3. Material data for typical AA6070 material tests.

| Temper | Orientation | $s_0$ (MPa) | $s_u$ (MPa) | $\sigma_{pt}$ (MPa) | $\varepsilon_f$ | $W_c$ (MPa) |
|---|---|---|---|---|---|---|
| | 0° | 51 | 139 | 243 | 0.79 | 151 |
| | 45° | 51 | 136 | 231 | 0.76 | 142 |
| | 90° | 50 | 138 | 225 | 0.66 | 118 |
| | 0° | 187 | 320 | 487 | 0.52 | 211 |
| | 45° | 186 | 328 | 474 | 0.46 | 180 |
| | 90° | 187 | 328 | 457 | 0.39 | 150 |
| | 0° | 373 | 393 | 475 | 0.26 | 115 |
| | 45° | 379 | 396 | 423 | 0.07 | 29 |
| | 90° | 387 | 399 | 416 | 0.04 | 19 |
| | 0° | 341 | 354 | 419 | 0.32 | 128 |
| | 45° | 346 | 360 | 396 | 0.14 | 55 |
| | 90° | 340 | 356 | 391 | 0.13 | 49 |

Table 4. Ballistic limit velocities and Recht-Ipson constants from experimental tests and finite element simulations.

| Temper | Experimental data | | | Numerical simulations | | | Deviation (%) |
|---|---|---|---|---|---|---|---|
| | $a$ | $p$ | $v_{bl}$ (m/s) | $a$ | $p$ | $v_{bl}$ (m/s) | |
| O | 1 | 1.94 | 348.0 | 1 | 1.94 | 296.0 | −14.9 |
| T4 | 1 | 2.05 | 506.2 | 1 | 2.05 | 438.1 | −13.5 |
| T6 | 1 | 2.21 | 562.5 | 1 | 2.21 | 480.6 | −14.6 |
| T7 | 1 | 2.20 | 529.1 | 1 | 2.20 | 438.3 | −17.2 |

Table 5. Optimised model parameters for different tempers of AA6070 (valid for the rolling direction).

| Temper | $A$ (MPa) | $Q_1$ (MPa) | $C_1$ | $Q_2$ (MPa) | $C_2$ | $W_c$ (MPa) | Mean square error |
|---|---|---|---|---|---|---|---|
| O | 38.8 | 79.5 | 56.9 | 88.2 | 4.0 | 151 | $2.4 \cdot 10^{-5}$ |
| T4 | 172.7 | 35.6 | 80.6 | 247.7 | 6.5 | 211 | $6.2 \cdot 10^{-5}$ |
| T6 | 350.0 | 30.1 | 185.9 | 72.8 | 7.7 | 115 | $9.4 \cdot 10^{-4}$ |
| T7 | 292.5 | 55.3 | 317.2 | 31.1 | 10.0 | 128 | $6.0 \cdot 10^{-4}$ |

Table 6. Physical constants and model parameters common to all tempers of AA6070.

| Temper | $E$ (MPa) | $\nu$ (-) | $\rho$ (kg/m$^3$) | $\alpha$ (K$^{-1}$) | $C_p$ (J/kgK) | $\dot{\varepsilon}_0$ (s$^{-1}$) | $c$ (-) | $\chi$ (-) | $T_r$ (K) | $T_m$ (K) | $m$ (-) |
|---|---|---|---|---|---|---|---|---|---|---|---|
| O, T4, T6, T7 | 70000 | 0.3 | 2700 | $2.3 \cdot 10^{-5}$ | 910 | $5 \cdot 10^{-4}$ | 0.001 | 0.9 | 293 | 893 | 1.0 |

Table 7. Results from CCET calculations.

| Temper | $\sigma_0$ (MPa) | $n$ | $B_0$ (-) | $C$ | $v_{bl}$ (m/s) | Deviation (%) |
|---|---|---|---|---|---|---|
| O | 51 | 0.213 | 3.63 | 0.0 | 332.4 | −4.5 |
| | | | | 0.142 | 357.3 | +2.7 |
| T4 | 187 | 0.166 | 2.99 | 0.0 | 498.0 | −1.6 |
| | | | | 0.117 | 528.4 | +4.4 |
| T6 | 373 | 0.050 | 2.64 | 0.0 | 562.9 | −0.1 |
| | | | | 0.103 | 593.1 | +5.4 |
| T7 | 341 | 0.036 | 2.69 | 0.0 | 534.7 | +1.1 |
| | | | | 0.105 | 563.9 | +6.6 |

Table 8. Data sets ($s_0, \varepsilon_f, W_c, \rho$), target thickness ($h$), areal mass ($m_A$), experimentally obtained ballistic limit velocities ($v_{bl}$) and kinetic energy at the ballistic limit ($E_{bl}$) for a number of materials impact by 7.62 mm APM2 bullets under identical conditions.

| Material | $s_0$ (MPa) | $\varepsilon_f$ | $W_c$ (MPa) | $\rho$ (kg/m$^3$) | $h$ (mm) | $m_A$ (kg/m$^2$) | $v_{bl}$ (m/s) | $v_{bl}/m_A$ (ms$^{-1}$/kgm$^{-2}$) | $E_{bl}$ (Nm) | $E_{bl}/m_A$ (Nm/kgm$^{-2}$) |
|---|---|---|---|---|---|---|---|---|---|---|
| AA6070-O | 51 | 0.84 | 151 | 2700 | 20 | 54 | 348 | 6.4 | 636 | 11.8 |
| AA6070-T4 | 187 | 0.53 | 211 | 2700 | 20 | 54 | 506 | 9.4 | 1344 | 24.9 |
| AA6082-T4 [34] | 195 | 0.53 | 199 | 2700 | 20 | 54 | 414 | 7.7 | 900 | 16.7 |
| AA5083-H116 [14] | 244 | 0.16 | 47 | 2700 | 20 | 54 | 492 | 9.1 | 1271 | 23.5 |
| AA6070-T7 | 341 | 0.32 | 128 | 2700 | 20 | 54 | 529 | 9.8 | 1469 | 27.2 |
| AA6070-T6 | 373 | 0.26 | 115 | 2700 | 20 | 54 | 563 | 9.9 | 1664 | 30.8 |
| AA7075-T651 [15] | 520 | 0.11 | 106 | 2700 | 20 | 54 | 628 | 11.6 | 2071 | 38.3 |
| NVE36 [39] | 335 | — | — | 7850 | 12 | 94.2 | 592 | 6.3 | 1840 | 19.5 |
| Weldox 500E [1] | 605 | 1.46 | 1516 | 7850 | 12 | 94.2 | 624 | 6.6 | 2044 | 21.7 |
| Weldox 700E [1] | 819 | 1.31 | 1486 | 7850 | 12 | 94.2 | 674 | 7.2 | 2385 | 25.3 |
| Hardox 400 [1] | 1148 | 1.16 | 2013 | 7850 | 12 | 94.2 | 741 | 7.9 | 2883 | 30.6 |
| Domex Protect 500 [1] | 1592 | 0.67 | 1484 | 7850 | 12 | 94.2 | 837 | 8.9 | 3678 | 39.0 |
| Armox 560T [1] | 1711 | 0.92 | 2310 | 7850 | 12 | 94.2 | 871 | 9.2 | 3983 | 42.3 |